

A NEW PORE-SCALE FRAMEWORK FOR THE SIMULATION AND INTERPRETATION OF WIDE-BAND DIELECTRIC MEASUREMENTS

Emmanuel Toumelin and Carlos Torres-Verdín, The University of Texas at Austin
Nicola Bona, ENI E&P

ABSTRACT

Conventional dielectric interpretation models explain dielectric dispersion in terms of factors such as ionic polarization due to grain or pore eccentricity, rock texture, fluid saturation, or even clay content. However, the same models fail to integrate all these factors simultaneously and bear no rigorous pore-level justification. We establish a comprehensive numerical framework to simultaneously incorporate geometrical and electro-chemical effects in the petrophysical assessment of wide-band electromagnetic measurements. The approach is successfully implemented on two-dimensional synthetic rocks. It allows the calculation of wide-band (kHz-GHz range) dispersions of conductivity and dielectric constant due to geometrical pore eccentricity, electromagnetic coupling, and double-layer polarization for different spatial configurations of pore, throat, and fluids. Our formulation is particularly suitable for core-scale electromagnetic upscaling, and can be parameterized with rock images, mercury injection data, and NMR measurements in order to improve the petrophysical assessment of rocks via wide-band dielectric dispersion.

INTRODUCTION

Because of their high sensitivity to rock texture and clay content, the potential of wide-band dielectric measurements for petrophysical characterization has been known for almost three decades. In the 1980s, at the time when dielectric studies were thriving, no alternative measurement could be used to refine and enrich the information provided by dielectric dispersion. As a result the method fell into a prolonged phase of stagnation. Recently, special emphasis has been made of the effect of thin wetting water films on wide-band dielectric measurements at low values of water saturation [1-3], which, together with new developments in other techniques and a better understanding of pore-scale phenomena, rekindles the possibility of accurate petrophysical characterization. This paper introduces a novel approach to model (and ultimately predict) characteristic petrophysical properties, including wettability, pore geometry and connectivity (and from them permeability to fluid flow), that influence the wide-band electromagnetic measurements of saturated rocks.

Beyond Mixing Laws

Several factors influence the dispersion of electrical properties (conductivity, σ , and relative dielectric permittivity, or dielectric constant, ϵ') measured on saturated rocks at

frequencies in the kHz-GHz range. One of the main difficulties in approaching the different existing models that attempt to explain these factors is that the two main schools of thought seem contradictory rather than complementary. Roughly speaking, geometric models use macroscopic shape-induced polarization (polarization models from Lysne [3] or mixing laws of type Bruggeman-Hanai [4-5]) to justify Maxwell-Wagner sigmoid frequency responses for the conductivity and the dielectric constant of saturated rocks. On the other hand, double-layer electrochemical models consider the microscopic motion of charged molecules around clays independently of general rock structure and geometry. Summaries of some of these processes can be found elsewhere [2-3, 6-8]. The ability to predict electrical dispersion curves from such individual models remains limited; hence marginal quantitative petrophysical information can be extracted from dielectric spectra. At the same time, the models provide no details of the actual rock geometry: it would be desirable to link the macroscopic features or pore and throat arrangements with the microscopic, yet important, thin wetting films and clay coatings. In this paper, we make use of remote-sensing electromagnetic concepts to introduce a numerical framework for the integration of these different petrophysical effects at the pore scale, together with information available from ancillary rock-core measurements.

Reconciling Wide-Band Remote Sensing Electromagnetics and Pore-Scale Dielectric Analytical Models

Remote-sensing electromagnetics, as used for instance in borehole geophysics, explicitly solves Maxwell's equations to propagate the response of dilute concentrations of electrical charge carriers (dilute ionic fluids in large-scale porous media) subjected to a given excitation. Analytical dielectric models, on the other hand, use chemical potentials and effective medium theories to predict mixture properties. Both approaches are conceptually different and are riddled with technical inconsistencies of their own, namely: (1) Maxwell propagation uses the duality of electric scalar potential and magnetic vector potential, while no equivalence exists for the magnetic vector potential in the electro-chemical potential formulation. (2) Effective medium theories or models based on single-grain geometries do not rigorously describe coherent interactions between scattering components (i.e., electromagnetic coupling of ionic brine inclusions in a resistive oil/rock mixture). (3) Components in mixtures are not symmetrically treated by mixing laws. (4) Small geometrical features, including wettability effects, are neglected by mixing laws. Geometrical models are based on microscopic anisotropy (ellipsoidal shapes of grains or pores), but still assume macroscopic isotropy. No core-scale anisotropy is included in mixing laws. (5) Effective medium theories fail to explain the dependence of dielectric measurements on brine (or sample) conductivity [4-5]. (6) Maxwell's equations alone fail to correctly reproduce the electrical response of a medium where ionic mobility is substantial, i.e., in high ionic concentrations close to charged surfaces/zeta potentials. Likewise, Maxwell's equations are not statistically justified when the dominant length of the geometrical domain is smaller than 10 nm [9].

In this paper, we show that shape-induced polarization can be accurately reproduced by solving Maxwell's equations in detailed rock/fluid geometries, thereby circumventing some of the conceptual deficiencies of effective medium theories. A minimum spatial

resolution of 10 nm is imposed to use Maxwell's equations, and an alternative analytical double-layer formulation can be used at the locations where brine occupies volumes of thickness smaller than 10 nm (thin films), or to describe presence of clays.

Methodology

Our purpose is to numerically describe pore geometries at the pore/throat scale, and to assess the relative importance of pore features neglected by dielectric mixing laws. As a first approximation, the porous medium is described as a two-dimensional (2-D) digital pore map that comprises brine inclusions embedded in a rock/oil compound (rock and oil having similar conductivity and dielectric constant in the kHz-GHz range). This digital map explicitly reproduces pore and throat geometries, anisotropy and multiphase saturations on a pixel basis, whereas effective volume complex conductivities for each pixel properly reproduce the effects of sub-pixel-scale features, including wettability and presence of charged clays. The pore map is treated as a scattering object *as a whole*, and exhibits *effective* values of conductivity σ_s and relative dielectric permittivity (or dielectric constant) ϵ_s' that vary with the frequency of the incident wave. The second main development deals with the inversion procedure to estimate σ_s and ϵ_s' . Electrical currents induced by the field incident on the detailed pore map are calculated via Maxwell's equations in the frequency domain. Subsequently, these currents are matched to those that *would* be obtained in a *homogeneous* scatterer subject to the same incident field, and the corresponding conductivity σ_s and dielectric constant ϵ_s' for that homogeneous medium become the effective properties of the 2-D digital rock at that frequency. Results for a variety of pore maps illustrate the effects of pore shape and connectivity attainable with our method beyond the limitations of dielectric mixing laws.

Conventions and Notation

We adopt the $e^{-i\omega t}$ harmonic convention for the incident electric field. The relative dielectric permeability, ϵ' , and the real conductivity, σ , measured at a given frequency, f , define a complex conductivity,

$$\sigma^* = \sigma - i \omega \epsilon' \epsilon_0, \quad (1)$$

where $i^2 = -1$, $\omega = 2\pi f$ is the angular frequency, and ϵ_0 is the vacuum dielectric permittivity. Likewise, a complex dielectric permittivity is defined as

$$\epsilon^* = \epsilon' \epsilon_0 + i \sigma / \omega = i \sigma^* / \omega. \quad (2)$$

Pixels describing the spatial distribution of rock/fluids are assigned individual conductivity values, e.g., σ_{grain}^* or σ_{water}^* , but the scatterer as a whole exhibits one macroscopic complex conductivity σ_s^* that remains the target of the inversion procedure. To simplify the problem at this preliminary stage, all conductivities are considered isotropic. With μ_0 described as the vacuum magnetic permeability, the wave numbers k_b and k_s are defined in the background and in the equivalent homogeneous scatterer, respectively, by Eq. (3):

$$k_{b,s}^2 = i\omega \mu_0 \sigma_{b,s}^* . \quad (3)$$

PROBLEM GEOMETRY

The geometry adopted for the pixel-based scatterer is chosen to be compatible with an existing analytical solution for a homogeneous dielectric and lossy medium on a wide frequency range (kHz-GHz). Previous developments [10] apply similar principles to numerically simulate the MHz-range response of 2-D pixel-based purely dielectric mixtures bounded by a waveguide, and compute the effective dielectric constant of the medium from the reflection and transmission coefficients at the scatterer boundaries. Those methods exhibit several disadvantages, namely: (a) the waveguide has to be meshed as well as the scattering medium, thereby decreasing the efficiency of the solution; (b) a reflection coefficient yields low-order approximations of the complex dielectric constant of a medium via its complex electrical impedance, and is tied to the angle of incidence of the wave at the scatterer surface; and, most importantly, (c) the waveguide method remains numerically accurate only below 80 MHz.

To circumvent the above limitations, we introduce an approach based on the disc-shape scatterer shown in Fig. 1. Without restriction on the frequency range, the medium is described as a disc populated with square pixels of contrasting conductivities and dielectric constants of grain and fluids representing the pore map. As summarized below, in the frequency domain, electromagnetic scattering by a homogeneous cylinder (in three dimensions) can be written as an expansion of cylindrical modes [11] that can be used as a fast forward model for the iterative inversion of effective properties for the detailed pixel-based scatterer.

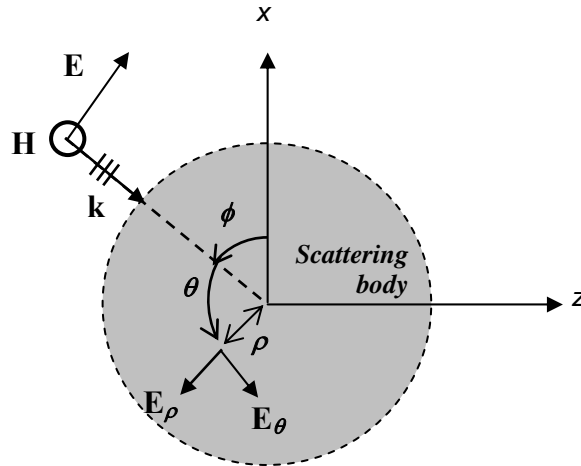


Fig. 1. Graphical description of the model geometry: incident transverse-electric (TE) polarized plane wave illuminating the 2-D scattering medium with an angle ϕ with respect to the x axis. E : incident electric field; H : incident magnetic field; k : wave (propagation) vector. (ρ, θ) are the polar coordinates of a point within the scatterer, with respect to the incident plane wave and the scatterer center, and (E_ρ, E_θ) are the polar electrical fields at that point.

Tradeoff between Spatial Resolution and Frequency

As frequency decreases from 1 GHz to 1 kHz, the circular boundary of the disc-shaped scatterer reduces boundary fringing effects, while a high-resolution pore map is necessary to damp these boundary effects at low frequencies for the case of resistive pixels. At the nm- to μm -scale resolution used in our study, attempts of pore maps with 255x255 pixels resolution exhibit substantial boundary fringing below 10 MHz for a homogeneous distribution of resistive pixels and 1 S/m background water. This results in erroneous post-inversion effective properties of the medium. If the resolution of the same medium increases to at least 401x401 pixels, however, the importance of boundary fringing decreases and the homogeneous properties are inverted properly from 10 kHz to 1 GHz.

Inclusion of Double-Layer Polarization

Our numerical approach implicitly encompasses all polarization effects due to shape and electromagnetic coupling between the water-filled pores (without charge accumulation). The case of polarization due to charge accumulation at the boundaries between rock and water is handled differently, but still included in our pixel-based framework. For this, objects surrounded by charge accumulation (e.g., clay grains or oil-filled pores with thin water films at the rock surface) are characterized by their sizes and shapes; micro-models are used to compute the frequency-dependent complex conductivity within each pixel corresponding to those objects. For instance, Lima and Sharma [12] used Fixman's [13] molecular-level solution of the double-layer polarization around a spherical grain with surface charges to characterize the frequency-dependent equivalent complex clay conductivity within clay areas. Here, we use the same molecular-level solution to compute the complex conductivity of clay pixels distributed in our pore-level 2-D digital rocks at each frequency. In this method, given a characteristic time τ in the order of 200 μs sufficient to build up a stationary charge around μm -size clay particles, and given a ratio of ion density at the clay surface and in the bulk water δ of the order of one, the complex clay conductivity is given by

$$\sigma_{clay}^* = \frac{\delta\sigma_w^*}{1 - \delta Y}, \quad \text{with } Y = \frac{1 + (1-i)\sqrt{\omega\tau}}{2 + 2(1-i)\sqrt{\omega\tau} - 2i\omega\tau}. \quad (4)$$

Figure 2 illustrates this frequency behavior for the dielectric constant of pure clay.

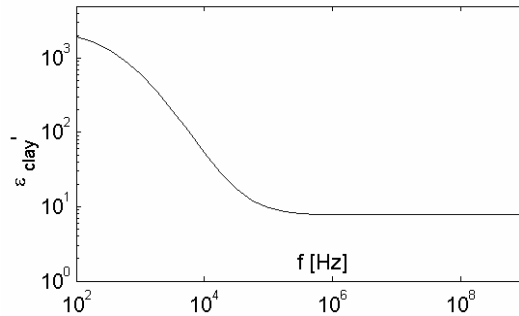


Fig. 2. Low-frequency dielectric enhancement of clays using Eq. (4) with $\tau = 200 \mu\text{s}$ and $\delta = 0.1$.

ELECTROMAGNETIC SCATTERING AND INVERSION OF EFFECTIVE CONDUCTIVITY AND DIELECTRIC PERMITTIVITY

Detailed Numerical Model on Pore Map

The Method of Moments (MoM) [14] was selected to solve Maxwell's equations in the detailed heterogeneous pore map for several reasons: (a) it uses the same frequency-domain as the fast analytical homogeneous solution used for effective property inversion; (b) it accurately and efficiently handles large contrasts in material electrical properties (as encountered at the water/grain contact); and (c) it allows large discretization grids in conjunction with Fast-Fourier transformation (FFT) and an iterative solver such as the Stabilized Bi-Conjugate Gradient [15]. The details of the FFT-MoM technique cannot be covered in this paper due to space limitations, however let us just mention that the method solves the general integral equation for the electric field \mathbf{E} at location \mathbf{r} , given by

$$\mathbf{E}(\mathbf{r}) = \mathbf{E}_b(\mathbf{r}) + \int_{\mathbf{r}' \in V_{scat}} i\omega\mu_0 \vec{\mathbf{G}}(\mathbf{r} - \mathbf{r}') \cdot \Delta\boldsymbol{\sigma}^*(\mathbf{r}') \cdot \mathbf{E}(\mathbf{r}') dV, \quad (5)$$

where \mathbf{E}_b is the background field imposed by the incident plane wave. The scatterer, here composed of rock and fluid pixels, occupies the volume V_{scat} and is characterized by its electrical conductivity contrast tensor $\Delta\boldsymbol{\sigma}^*$ with respect to the water background. In this paper, $\Delta\boldsymbol{\sigma}^*$ is considered isotropic and therefore becomes the scalar $\Delta\sigma^* = \sigma_s^* - \sigma_b^*$ according to Eq. (1), i.e., $\Delta\sigma^* = 0$ where the pixels are water and $\Delta\sigma^* = \sigma_{grain}^* - \sigma_{water}^*$

where they are grains. For completeness, we emphasize that $\vec{\mathbf{G}}$ is the dyadic Green's tensor for the electrical field and is here integrated analytically on the rectangular cells of the pore maps [16].

Fast Analytical Model of a Homogeneous Cylinder

Following the standard modal expansion of a TE plane wave and of the electromagnetic fields scattered by a homogeneous cylinder [11], one obtains the analytical solution for the electric field components inside the cylinder in polar coordinates. They are, respectively:

$$E_\theta(\rho) = i\sqrt{\frac{\mu_0}{\epsilon_s^*}} H_0 \left\{ B_0 J_1(k_s \rho) - 2 \sum_{n \geq 1} (-i)^n B_n J_n'(k_s \rho) \cos(n\theta) \right\} \quad (6a)$$

for the tangential electric field, and

$$E_\rho(\rho) = -\frac{2i}{\omega\epsilon_s^* \rho} H_0 \sum_{n \geq 1} n (-i)^n B_n J_n(k_s \rho) \sin(n\theta) \quad (6b)$$

for the radial electric field. In these expressions, ρ is the distance from the cylinder center to a point inside the homogeneous cylinder and θ is the angle between that point, the cylinder center, and the direction of the incident field (see Fig. 1). The coefficients B_n are determined from the boundary conditions at the cylinder of radius a , and are given by

$$B_n = \frac{A_n H_n^{(1)}(k_b a) + J_n(k_b a)}{J_n(k_s a)}, \quad (7a)$$

where

$$A_n = \frac{\sqrt{\varepsilon_b^*} J_n(k_b a) J_n'(k_s a) - \sqrt{\varepsilon_s^*} J_n(k_s a) J_n'(k_b a)}{\sqrt{\varepsilon_s^*} J_n(k_s a) H_n^{(1)'}(k_s a) - \sqrt{\varepsilon_b^*} H_n^{(1)}(k_b a) J_n'(k_s a)}. \quad (7b)$$

In Eqs. (6)-(7), J_n is the Bessel function of the first kind, J_n' its derivative, $H_n^{(1)}$ the Hankel function of the first kind, and $k_{b,s}$ designates the wavenumber in each homogeneous medium (background or scatterer, respectively).

The normalizing factor H_0 is obtained by equating the incident electric field at the center of the cylinder to its harmonic components. Projection of the polar-coordinate form given by Eqs. (6), together with consideration of both the angle of plane-wave incidence ϕ and the position angle θ yields the analytical Cartesian coordinates of the electric field within the homogeneous cylinder, \mathbf{E}_h .

Inversion of Effective Conductivity and Dielectric Permittivity

Recalling the integral equation (5), the electrical field propagated to any location in space is a weighted function of the currents \mathbf{J} inside the scatterer, i.e.,

$$\mathbf{J} = \Delta\sigma^* \mathbf{E} \quad (8)$$

where $\Delta\sigma^* = \sigma_s^* - \sigma_b^*$ is the conductivity contrast of the homogeneous scatterer with respect to the background. To enforce Maxwell's equations, the effective real conductivity σ_s and relative dielectric permittivity ε_s' are chosen to minimize the quadratic norm of the residual between (a) these equivalent currents taken over the entire homogeneous disc $\mathbf{J}_h = (\sigma_s - i\omega\varepsilon_s'\varepsilon_0 - \sigma_b^*) \mathbf{E}_h$, and (b) the currents calculated over the detailed numerical model of the heterogeneous pore map.

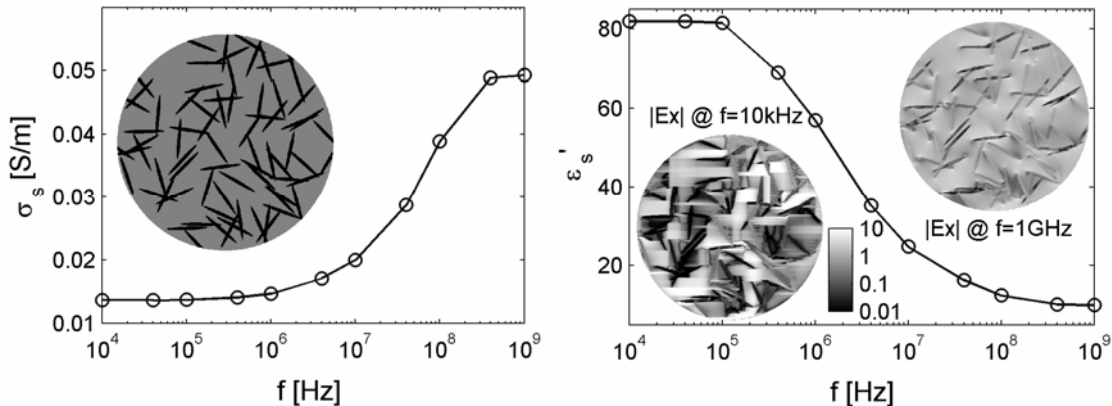


Fig. 3. Effective conductivity (left panel) and dielectric permittivity (right panel) computed for inclusions of water ellipses (left panel, insert). Inserts (right panel) illustrate the effect of frequency on the amplitude of the electric field within the medium.

EXAMPLES OF APPLICATION

We illustrate our new numerical approach with a few examples based on binary rock/water maps of 401x401 and 501x501 pixels with 1 μm pixel resolution (results are independent of that resolution). The rock phase is assigned quartz properties ($\varepsilon' = 4.5$ and $\sigma = 0$), and water is assumed a saline brine ($\varepsilon' = 78$ and $\sigma = 1 \text{ S/m}$).

Numerical Simulation of Maxwell-Wagner-Type Polarization

We first consider a medium whose effective electrical response takes the form of smooth sigmoids for both conductivity and dielectric permittivity (Fig. 3), as predicted by the Maxwell-Wagner theory. As illustrated by this figure, the magnitude of the electric fields within the scatterer responds to the geometrical distribution of conductivities (water vs. rock grains) at high frequencies, while at low frequencies both the spatial resolution of the internal electric fields and the correlation between electric field contrast and conductivity contrast decrease. Such is the origin of the wide-band polarization that is here simulated fully numerically. In this example, the effective dielectric constant at low frequencies is larger than the higher dielectric constant of the mixture constituents (78 for water). This effect is typical of high pore and grain eccentricities encountered by an incoming wave.

Asymptotic Rules for DC Conduction and High-Frequency Dielectric Constant

Archie's first law for DC conductivity and the volumetric CRIM (Complex Refractive Index Method) model for the dielectric constant of saturated rocks are well-established asymptotic rules in Petrophysics. These equations are:

$$\text{Archie:} \quad \sigma_{DC} = \sigma_w \phi^m, \text{ with } m \approx 2 \quad (9)$$

$$\text{CRIM:} \quad \sqrt{\varepsilon'_{eff}} = \sum_{\text{component } i} \phi_i \sqrt{\varepsilon'_i}. \quad (10)$$

In Eq. (10), ϕ_i is the fractional volume assigned to phase i in the mixture. Comparison of these rules against the asymptotic values of the numerically simulated values of σ_s and ε'_s provides insight to their conditions of application. Corrections can be suggested depending on the rock model.

Wide-Band Shape Polarization, Electromagnetic Coupling and Water Percolation

Pore maps exhibiting water inclusions of different eccentricities at 8 and 20% porosity, shown in Fig. 4, are used to assess shape polarization effects. At very low values of porosity (dilute concentration of water inclusions), little collective influence (or coupling) is expected between the water-filled inclusions; mixing laws predict an enhancement of both the high-frequency conductivity and the low-frequency dielectric constant with increasing values of inclusion aspect ratio. Figure 5 shows for the 8%-porosity examples that such a trend is respected, even though the dielectric permittivity curves do not exhibit a smooth sigmoid shape, but rather include several inflection points between 1 and 100 MHz. This is due to the influence of electromagnetic coupling which has an impact for values of porosity as low as 8% in 2 dimensions. When porosity increases to

20% (Fig. 6), similar trends are observed, except for the amplitudes of σ_s and ϵ_s' which are higher. In cases D and E, no percolation of the water phase throughout the medium has been reached, and their low-frequency conductivity values are very close, around 0.002 S/m. In case F, water percolation is close and the low-frequency σ_s increases correspondingly to 0.014 S/m. In the latter case, it is also noticeable that the dielectric dispersion now exhibits a smooth sigmoid shape with only one inflection point around 10 MHz. In all the cases A-F, the high-frequency dielectric constant remains close to that of

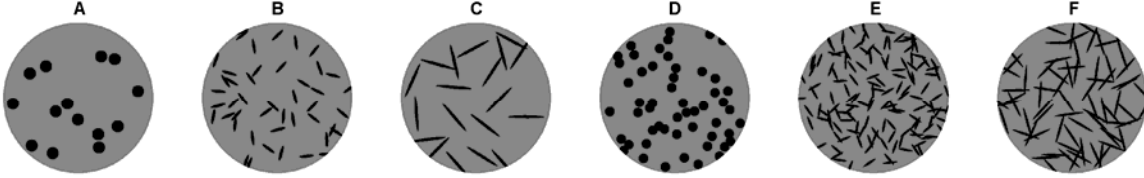


Fig. 4. Examples of 2-D rock models based on water inclusions (black pixels) embedded in a rock host (gray pixels). Maps A to C exhibit 8% porosity, and maps D to F, 20%. Each pore map consists of randomly distributed inclusions with uniform eccentricity, e ; for maps A and D: $e=1$ (discs); B and E: $e=4$ (ellipses); C and F: $e=8$ (ellipses).

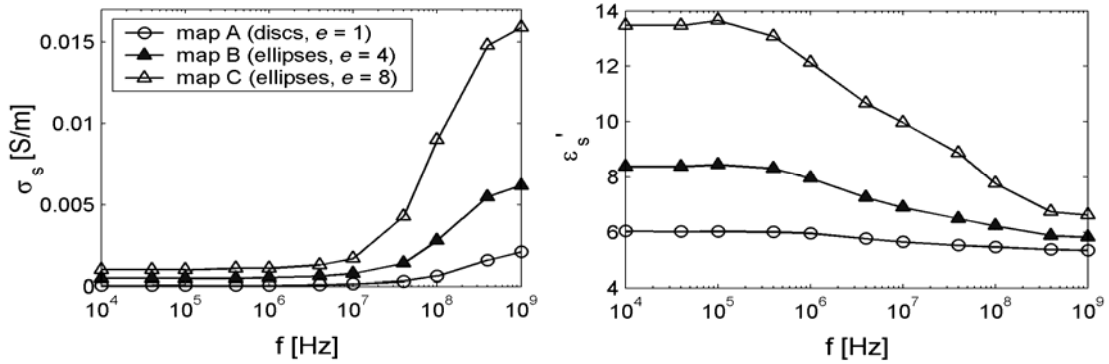


Fig. 5. Comparison of effective conductivity (left panel) and dielectric permittivity (right panel) computed for 8%-porosity water inclusions with different shapes ($\sigma_{Archie}=0.007$ S/m and $\epsilon'_{CRIM}=7$).

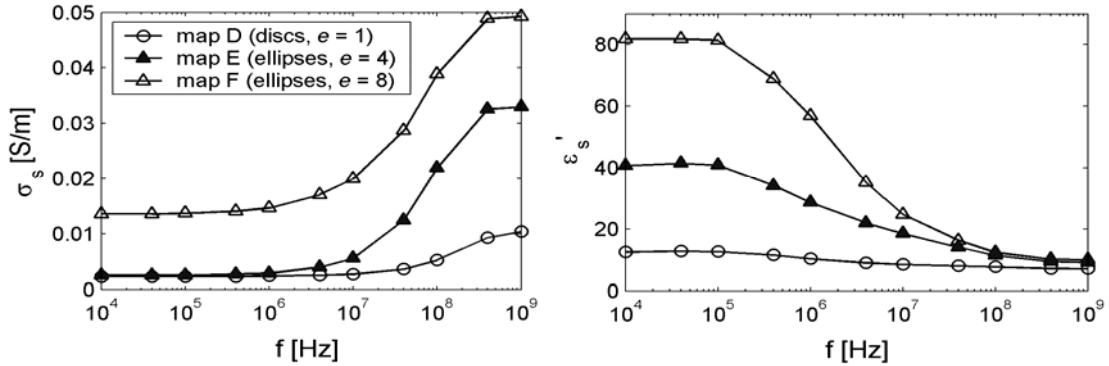


Fig. 6. Same as in Fig. 5 but for 20%-porosity models ($\sigma_{Archie}=0.04$ S/m and $\epsilon'_{CRIM}=12$).

the CRIM estimate, while the only case close to Archie's conductivity magnitude is that of the near-percolating case F.

Pore Texture and Connectivity

Turning to more realistic rock morphologies, four other 2-D rocks G to J (Fig. 7) were designed with different pore arrangements and connectivities. As illustrated by Fig. 8, 8%-porosity pore maps C and G exhibit similar dielectric enhancements from about $\epsilon_s' = 7$ at 1 GHz up to about 14-15 at 10 kHz, although the pore shapes are much different and

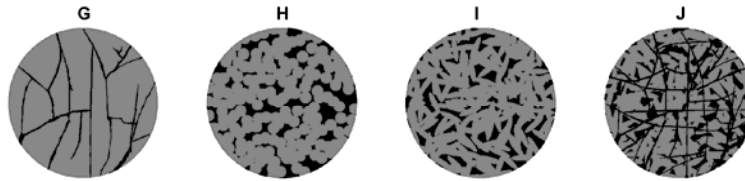


Fig. 7. Additional binary rock maps designed for the study of rock texture effects. Map G: throat arrangement between grain blocks ($\phi=8\%$); H: disconnected pore space remaining between disc grains ($\phi=20\%$); I: same as B but with elliptical grains; J: well-connected pore/throat system ($\phi=25\%$).

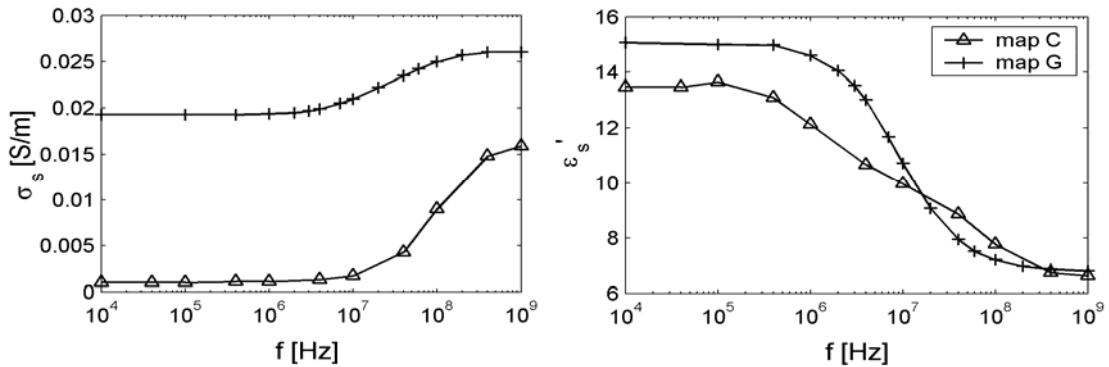


Fig. 8. Effective conductivity (left) and dielectric permittivity (right) computed for rock models C and G, both exhibiting 8% porosity ($\sigma_{Archie} = 0.007$ S/m and $\epsilon'_{CRIM} = 7$).

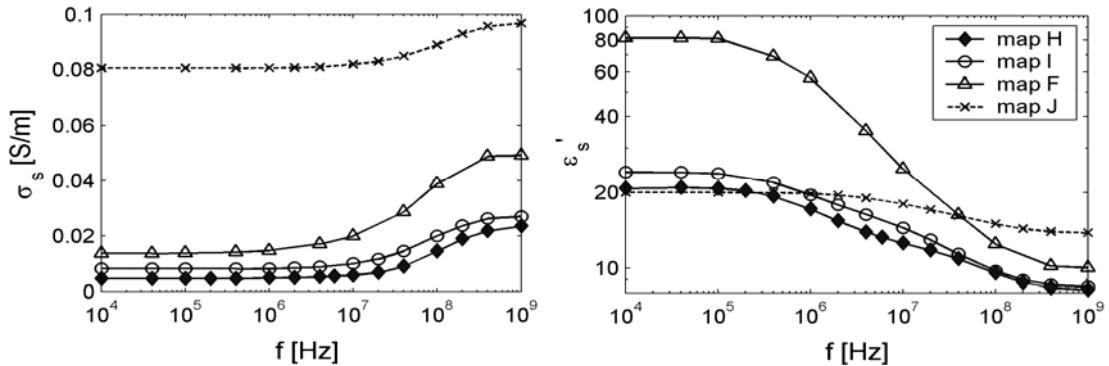


Fig. 9. Same as in Fig. 8 for models F, H, I ($\phi=20\%$, $\sigma_{Archie} = 0.04$ S/m, $\epsilon'_{CRIM} = 12$), and J ($\phi=25\%$).

map G exhibits better connectivity. The conductivity dispersions in Fig. 8 clearly show this difference in connectivity (that of map G is much higher), but the dielectric dispersion includes additional information in the form of different inflection points (one around 10 MHz for the smooth sinusoid of map G, two for map C around 300 kHz and 50 MHz). In the absence of accurate measurements of brine salinity or saturation (such as in downhole measurements), dielectric spectral information could be useful. Figure 9 shows the results for 20%-porosity cases, and illustrates the complementarity of several characteristic features, namely, the value of the low-frequency conductivity, the value of the enhancement of both ε_s' at low frequency and σ_s at high frequency, and the shape of the dielectric dispersion in its MHz-range transition. The most connected rock models exhibit smooth sigmoid-shape dielectric dispersions (maps F and J), even if the effective conductivity is not significantly higher than for the non-percolating cases (case F vs. I). The most conductive case, J, is also the one which exhibits the least dielectric enhancement, thereby indicating that both quantities are not related. Finally, cases I and J mainly differ by the inflection of their corresponding dielectric dispersion below 100 MHz. In all those cases, both σ_{Archie} and ε'_{CRIM} are honored only when connectivity exists between pores.

APPLICATION TO CORE SCALE-UP

The numerical method can handle at most 1 Megapixel, therefore a multi-scale approach can be devised to incorporate accurate petrophysical information in the model. Digital rock pictures provide information on the grain/pore arrangement that can be selected to locate the main pores, in a manner similar to pore maps H and I, with a resolution in the order of 10 μm . NMR can also be effectively used to delineate the pore-size distribution within the sample. Then, each pixel of this large-scale model becomes a micro-model for more accurate pore/throat/fluids arrangements, which can now reach 10-nm resolution and can be constrained by resistivity and mercury injection data. Higher values of spatial resolution are no longer amenable to Maxwell's equations and, therefore, require the treatment of isolated analytical micro-models.

CONCLUSIONS

Recent advances in computational resources and efficient numerical algorithms allow the explicit computation of wide-band electromagnetic polarization of saturated rocks. Consequently, the effect of detailed pore structure on rock electromagnetic measurements can be studied in unprecedented detail. This method enables the quantitative analysis of the electromagnetic response of pore/throat/fluids geometries, whereas the development of electrical anisotropy inversion yields accurate and reliable results not achievable with effective medium theories or standard mixing laws. Specifically, the numerical model developed in this paper (a) has the ability to discriminate the origin of low-frequency dielectric enhancements that can be due to both charged clay and thin fluid films, (b) properly describes the wide-band effect of pore texture, connectivity, fluid distribution and percolation, and (3) allows the inclusion of electrical anisotropy at the core scale.

ACKNOWLEDGEMENTS

Guozhong Gao is acknowledged for his help in implementing the 2D-MOM FFT method for large numerical grids. Funding for the work reported in this paper was provided by (a) the American Chemical Society through grant no. PRF 37519-AC9, (b) the US Department of Energy through contract no. DE-FC26-04NT15518, and (c) UT Austin's Research Consortium on Formation Evaluation, jointly sponsored by BP, Baker Atlas, ConocoPhillips, ENI E&P, ExxonMobil, Halliburton Energy Services, Mexican Institute for Petroleum, Occidental Oil and Gas Corporation, Petrobras, Precision Energy Services, Schlumberger, Shell International E&P, Statoil, and Total.

REFERENCES

1. Bona, N., E. Rossi, C. Venturini, S. Cappaccioli, M. Lucchesi, and P. Rolla, "Characterization of rock wettability through dielectric measurements," *Revue de l'Institut Français du Pétrole*, (1998) **53**, 6.
2. Bona, N., E. Rossi, and S. Capaccioli, "Electrical Measurements in the 100 Hz to 10 GHz Frequency Range for Efficient Rock Wettability Determination," *SPE Journal* (2001), March.
3. Bona, N., A. Ortenzi, and S. Capaccioli, "Advances in understanding the relationship between rock wettability and high-frequency dielectric response," *Journal of Petroleum Science and Engineering*, (2002) **33**.
4. Sen, P., C. Scala, and M. Cohen, "A self-similar model for sedimentary rocks with application to the dielectric of fused glass beads", *Geophysics*, (1981) **46**.
5. Kenyon, W., "Texture effects on megahertz dielectric properties of calcite rock samples," *Journal of Applied Physics*, (1984) 55, 8.
6. Olhoeft, G., "Low-frequency electrical properties," *Geophysics*, (1985) **50**, 12.
7. Myers, T., "A saturation interpretation model for the dielectric constant of shaly sands," 1991 SCA Conference paper number 9118.
8. Sihvola, A., (Ed.), *Electromagnetic Mixing Formulae and Applications*, IEE Electromagnetic Waves Series 47, London, U.K., (2002).
9. Jackson, J., *Classical Electrodynamics*, 2nd edition, Wiley, (1975), 227-228.
10. Pekonen, O., K. Kärkkäinen, A. Sihvola, and K. Nikoskinen, "Numerical testing of dielectric mixing rules by FDTD method," *Journal of Electromagnetic Waves and Applications*, (1999) **13**, 1.
11. Balanis, C, *Advanced Engineering Electromagnetics*, Wiley, (1989), 608-610 and 666-667.
12. Lima, O., and M. Sharma, "A Generalized Maxwell-Wagner Theory for Membrane Polarization in Shaly Sands", *Geophysics*, (1992) **57**, 3.
13. Fixman, M., "Charged macromolecule in external fields. I. The sphere," *Journal of Chemical Physics*, (1980) **72**, 9.
14. Wang, J., *Generalized Moment Methods in Electromagnetics*, Wiley, (1990).
15. Sleijpen, G.L.G., and D.R. Fokkema, "BiCGstab(L) for linear equations involving unsymmetric matrices with complex spectrum," *Electronic Transactions on Numerical Analysis*, (2003) **1**, 11-32, September issue.
16. Gao, G., C. Torres-Verdín, and T. Habashy, "Analytical techniques to evaluate the integrals of 3D and 2D spatial dyadic Green's functions," *Progress in Electromagnetics Research (PIER)*, (2005) **52**, 1, 47-80.